Metallic skeleton promoted two-phase durable icephobic layers

Jie Wang[a], Mengjuan Wu[a], Junpeng Liu[a], Fang Xu[a], Tanvir Hussain[a], Colin Scotchford[a] and Xianghui Hou[a]*

[a] Faculty of Engineering, University of Nottingham, University Park, Nottingham NG7 2RD, UK;

* Correspondence: xianghui.hou@nottingham.ac.uk; Tel: +44-115-95-13920

ABSTRACT

Hypothesis: The accretion of ice on component surfaces often causes severe impacts or accidents in modern industries. Applying icephobic surface is considered as an effective solution to minimise the hazards. However, the durability of the current icephobic surface and coatings for long-term service remains a great challenge. Therefore, it is indeed to develop new durable material structures with great icephobic performance.

Experiments: A new design concept of combining robust porous metallic skeletons and icephobic filling was proposed. Nickel/polydimethylsiloxane (PDMS) two-phase layer was prepared using porous Ni foam skeletons impregnated with PDMS as filling material by a two-step method.

Findings: Good icephobicity and mechanical durability have been verified. Under external force, micro-cracks could easily initiate at the ice/solid interface due to the small surface cavities and the difference of local elastic modulus between the ice and PDMS, which would promote the ice fracture and thus lead to low ice adhesion strength. The surface morphology and icephobicity almost remain unchanged after water-sand erosion, showing greatly improved mechanical durability. By combining the advantages of the mechanical durability of porous Ni skeleton and the icephobicity of PDMS matrix, the Ni foam/PDMS two-phase layer demonstrates great potentials for ice protection with long-term service time.

Key Words: Ice protection; Porous Ni skeleton; Polydimethylsiloxane (PDMS); Surface cavities; Two-phase structures; In-situ icing.

1. Introduction

Undesirable icing phenomena including ice formation and accretion often cause serious impacts in industries and normal lives. Unpredictable ice accretion could even result in disastrous consequences in certain situations such as transportation, infrastructure, wind turbines, and power line transportation, etc [1-4]. To mitigate the icing hazards on concerned surfaces is of great significance, and intensive attention has been paid to the icephobic surfaces over the last decade [5, 6].

It is believed that superhydrophobic surfaces could help to repel water droplets away and prevent or delay ice nucleation, for the reason that the hierarchical structures and low surface energy introduce high-energy barriers and thermal barriers for ice formation [7-9]. However, the hierarchical micro/nano structures of superhydrophobic surface and coatings would inevitably lead to vapour condensation under a high humidity environment involving high-velocity water droplet impact [10, 11]. This could pose significant challenges to maintain the thermodynamic stability of surface icephobicity.

Enlightened by the slippery pitcher plants that repel liquid and solid, slippery liquid infused porous surface (SLIPS) has been recently developed for its impressive icephobic capability [12-14]. The low ice adhesion strength of SLIPS prompts its potentials in icephobic applications. Various types of oils have been chosen as lubricants and applied on different substrates to fabricate SLIPS. For example, Kim et al. prepared SLIPS-coated Al surface by infusing a water-immiscible liquid into a chemically functionalized nanostructured surface, which suppressed ice/frost accretion and provided lower ice adhesion compared to reference materials [15]. Irajizad et al. studied magnetic slippery surfaces (MAGSS) by exploiting magnetic force to induce a liquid-liquid interface [16]. These surfaces show great icephobicity with an ice adhesion strength of 2 Pa and 2-3 orders of magnitude extended ice formation time.

However, the mechanical durability of SLIPS in long-term service would inevitably be limited by the surface liquid nature. The depletion of the lubricants remains a serious problem during applications [17-19]. It is of significance for icephobic surfaces to keep long-term durability in severe mechanical and erosive environmental conditions. The current development of durable and reliable icephobic surfaces remains elusive. For example, Wang et al. reported a new nanostructure design that could realise robust superhydrophobicity by structuring surfaces at two different length scales to provide water repellency and durability [20]. The interconnected surface frame could act as “armour” and house the mechanically fragile and hydrophobic nanostructures. Irajizad et al. fabricated a new type of icephobic material composed of silicone elastomer matrix with high shear modulus and dispersible silicon-based organogel having low shear modulus [21]. The surface shows fairly low ice adhesion that is derived from the crack initiation based on the stress-localisation concepts. However, a durable icephobic surface with good erosion resistance in long-term harsh service environment still remains deficient.

In this work, we proposed a new design concept of combining robust porous metallic skeletons and icephobic filling to construct a two-phase layer structure, which demonstrated good icephobicity with excellent mechanical durability. Nickel (Ni) foam was chosen as the porous skeleton (phase I), and Polydimethylsiloxane (PDMS) was selected as the filling material (phase II). Ni foam/PDMS layers with fine surface cavities were prepared by a two-step method. The results showed that the two-phase structure could maintain very low ice adhesion after erosion impact which was attributed to the icephobic PDMS layer and the micro-crack initiation mechanism, and the introduction of Ni porous skeleton significantly prompted the surface durability under the erosion impact. The Ni foam/PDMS layer combines the mechanical advantages of Ni skeleton and the icephobicity of PDMS, providing an alternative concept for designing icephobic surfaces.

2. Experimental

2.1 Materials

Porous nickel (Ni) foam was obtained from TMAX Battery Equipment Ltd (Xiamen, China), with a thickness of 0.3 mm and a porosity of around 90%. Polydimethylsiloxane (PDMS) R-2180 was purchased from NuSil Technology (High Wycombe, UK), and xylene was supplied by Fisher Scientific UK Ltd (Loughborough, UK). 304 stainless steel (SS) plates were chosen as the reference substrates.

2.2 Sample preparation

The porous skeleton was cut into rectangular plates with a dimension of 50 mm × 20 mm. The plates were cleaned thrice using acetone and deionised water using ultrasonic bath and then dried out with compressed air. For 304 SS substrates, sandblasting was conducted before the coating preparation.

To prepare Ni foam/PDMS samples, two parts of the PDMS resin (Part A: 5g in 5 ml xylene, the same ratio for Part B) was dissolved in xylene separately and magnetically stirred, respectively. Then the two solutions were mixed together using magnetic stirring for 1h, prior to the PDMS impregnation. The Ni foam plates were fully immersed into the mixture solution and transferred into a vacuum oven (Vacutherm, ThermoFisher, Waltham, MA USA) (0.05 bar) for 30 min to degas existing air inside the porous structure, followed by post-baking at 75 °C for 45 min (to remove solvent) and 150 °C for 135 min (elevated temperature cure). The degassing process would ensure a full impregnation of the PDMS resin into the porous Ni skeletons.

After impregnation and curing, additional PDMS was applied onto the sample surface using the same mixture solution and spin-coated (KW-4A, Chemat Group, Northridge, CA,

USA) at a speed of 1500 RPM for 1 min. The samples were then heated in the vacuum oven for a similar post-baking treatment. For comparison purposes, a PDMS layer was coated onto sandblasted 304 SS substrates using spin coating with the same coating and post-baking treatment conditions.

Four types of samples had been prepared in this work: as-received porous Ni foam plates were abbreviated as AR-Ni, Ni foam/PDMS samples were designated as Ni/PDMS-S, the samples immediately after impregnation and curing without the additional spinning process were named as Ni/PDMS-A, and PDMS coating on 304 SS substrate was designated as SS-PDMS.

2.3 Microstructural characterisation

Surface morphologies of the samples were investigated by a scanning electron microscopy (SEM, JEOL-6490LV). 3D surface topography and surface roughness of the samples were obtained using a non-contact optical profiler (Zeta-20, KLA-Tencor). The chemical compositions and binding energy of the surface elements were characterised by an X-ray photoelectron spectroscopy (XPS) (Kratos Analytical Ltd).

2.4 Wettability and icephobicity tests

Water contact angle of the surfaces was measured by a contact angle goniometer (FTA200, First Ten Angstroms, Inc.) using a micro-pipette at room temperature and humidity condition. Static water contact angle was measured with fixed droplet volume of 5 μL and pumping out rate of 1 μL/s. For dynamic water contact angle measurement, water pumping out rate of 0.05 μL/s was used, similar to the testing condition reported by Esmaeili et al. [22]. Several repeating measurements were conducted to ensure data accuracy.

Electro-thermal de-icing test was performed to evaluate the de-icing performance of the different samples. An experimental apparatus was set up according to our previous work [23]. The test was conducted in a cold chamber set at -5 ± 0.2 °C. A pre-prepared glaze ice block (20 mm × 20 mm × 20 mm) was frozen onto the sample surface and held downward in the test. Electro-thermal heating was applied with an input voltage of 22 V and a current of 0.13 A. The duration of heating and the temperature change were recorded until the ice block was detached from the sample surface. The overall energy consumption for the de-icing could be calculated accordingly, to evaluate the de-icing efficiency of the sample. For each tested sample, three parallel tests were carried out to ensure data accuracy.

The ice adhesion strength was measured using a centrifugal system with a controlled glaze ice block attached to the sample surface at -10 °C in an environmental chamber (Design Environmental ALPHA 1550-40H) [24]. A silicone mould was fully filled with 1.31 ml deionised water and carefully covered onto the sample surface. Then the samples were kept inside the environment chamber at -10 °C for 24 h, to form glaze ice on the sample surface. With a certain value of centripetal acceleration on the sample, which was induced by the rotor rotation, the glaze ice cube would overcome the adhesion strength and detach from the sample. The ice adhesion strength could be calculated by the equation below:

$$F = mr\omega^2 \tag{1}$$

Where ω is the speed of rotation (rad/s) at the ice detachment, r is the length of the rotor (m), m is the mass of ice (kg) and F is the centrifugal force (N). The shear stress can be determined by:

$$\tau = F/A \tag{2}$$

Where A is the contact area (m^2), and τ is the shear stress (Pa). Five ice adhesion strength tests were carried out using parallel samples to ensure data accuracy.

2.5 ESEM Observation of In-situ icing process

In-situ icing process was observed by an environmental scanning electron microscopy (ESEM) equipped with a Peltier cooling stage (FEI Quanta 650, ThermoFisher). ESEM can image hydrated samples using a differential pumping system and gaseous secondary electron detector. In ESEM, adjusting the pressure of the water vapour in the specimen chamber, and the temperature of the cooling stage would allow the water to condense on the sample surface. In this work, the water condensation and in-situ icing process of the samples were recorded, at temperature of -5.0 ± 2.0 °C and relative humidity of 90 ± 5%.

2.6 Durability tests

To evaluate the sample durability, water-sand impinging erosion tests were conducted using a rig described previously [25] under pressurized pneumatic water-sand (SiC, SC224, Silicon Carbide 600 Finer powder, Simba Materials Ltd, Doncaster, UK) suspension (sand ratio 1 wt%) impinging with gas pressure of 103.4 kPa, velocity of 37 m/s, and liquid flow rate of 72 mL/min. One test lasted 90 min. The distance between the nozzle (with a diameter of 2 mm) and the tested sample was kept at 4 cm. The surface morphology and icephobicity of the samples were evaluated before and after the erosion test.

3. Results and discussion

3.1 Microstructures of the samples

Fig.1 shows the SEM surface morphologies of AR-Ni, Ni/PDMS-A, and Ni/PDMS-S. The cross-sectional image of AR-Ni is also provided. Fig.1a is the surface morphology of AR-Ni. It clearly shows the highly porous structure of the Ni foam, and the calculated porosity is around 89.1%. Here, the porosity of AR-Ni could be obtained by calculating the ratio between the actual weight of AR-Ni and the theoretical weight of solid Ni with the same dimension. The Ni foam provides the skeleton for the impregnation of icephobic substances. It is expected that the Ni foam skeleton could play important roles in enhancing the durability to extend the service life. Fig.1b is the cross-sectional image of AR-Ni, similar to its porous surface morphology. Fig.1c is the SEM image of Ni/PDMS-A. It is observed that some of the internal porosity has been filled, while some sharp and deep surface pores remain on the surface. The porosity of Ni/PDMS-A has been calculated with a value of 21.4%. From XPS spectrum analysis, no Ni element could be detected on the surface, indicating that all Ni foam skeleton has been fully covered by PDMS layer, as indicated in Fig.S1 (Supplementary Material). The unfilled sharp and deep surface pores could be an issue for the de-icing process [26]. Fig.1d is the SEM image of Ni/PDMS-S, showing that the big pores on the surface have been filled by PDMS, leaving some fine and shallow surface cavities. And no sharp metallic feature is observed, while the profile of the Ni skeleton could still be reflected from the image. The porosity of Ni/PDMS-S reduces to only 11.6%, with a measured Ra value of 24.1±0.9 μm. The size of the surface cavities is around 100 to 300 μm and the depth ranges from 50 to 150 μm, measured from the surface profilometer, as shown in Fig.S2 (Supplementary Material).

3.2 Wettability of the Ni foam/PDMS samples

Tab.1 shows the surface wettability of the different samples, including water contact angle (WCA), advancing angle (Adv), receding angle (Rec), and contact angle hysteresis (CAH). The WCA of AR-Ni could reach 131.4±3.2° while its CAH is only 7.8±0.1°. The highly rough structure introduces the time-dependent wettability to the AR-Ni and presents the Cassie-Baxter wetting mode. However, this hydrophobicity is metastable and would be easily deteriorated as the high WCA is mainly attributed to surface gaseous adsorption in air [27]. Ni/PDMS-A has a lower WCA of 121.9±2.5° and CAH of 8.5±0.1°, contributed from the very rough surface constructed by the Ni foam skeleton and the PDMS filling. For Ni/PDMS-S, with an additional PDMS layer on top and shallow surface cavities, the static WCA is 112.9±2.4° with CAH of 14.1±0.1°, which is very close to the inherent WCA value of pure flat PDMS. The flattened and shallow surface cavities on Ni/PDMS-S result in a slight decrease in water contact angle.

3.3 Water condensation and icing study

The water condensation and ice formation at subzero temperature were studied on Ni/PDMS-A using ESEM. In Fig.2a, the surface pores are full of condensed water, both on the top edges and at the bottom. It is found that no ice crystal nucleates on the surface by desublimation under the condition of T ≈ -7.1 °C and relative humidity (RH) ≈ 88.0%. This observation indicates the delayed icing nucleation on the formed structure surface, with the supercooled water. As temperature decreases, ice nucleation could take place in certain circumstances. After 8 s, the ice formation could be observed in Fig.2b. At the moment of ice formation, a great deal of latent heat generated in the phase transformation from water to ice would be released and a sudden temperature increase would occur. The condensed supercooled

droplets on the surface pores close to the Ni foam skeleton (bottom left corner) become ice crystals, while the water at the bottom of the surface pores remains liquid form, showing a state of water-ice co-existence. It could be assumed that the ice nuclei have a preference to form in the surface pores near the Ni foam skeleton. Once the ice forms, the nucleus grows rapidly. More ice nucleation points have been observed at the positions close to Ni foam skeleton covered by PDMS layer. It is found that most of the ice nuclei are close to the Ni foam skeleton and no ice nucleation is observed at the bottom of the pores, as indicated in Fig.2c. Then from Fig.2c to Fig.2e, the condensed supercooled droplets at the bottom of pores also turn into ice after 16 s. From Fig.2e to Fig.2f, the ice crystals keep growing and could form randomly around the area of Ni foam skeleton which further leads to ice interlocks.

It is interesting to note that the accretion of the ice crystals from the supersaturated vapours on the rough surface of Ni/PDMS-A seems to be quite obvious which has been evidenced by the severe mechanical interlock around the Ni foam skeleton during the water sublimation under reduced vapour pressure, as shown in Fig.S3a and Fig.S3b (Supplementary Material). It is indicated that ice nearly exists in all of the available areas between the sharp and deep surface pores. The red frames in Fig.S3 clearly corroborate the interlocked ice. Especially in Fig.S3b, the formed ice around the Ni foam skeleton would cause a lot of difficulties in the ice removal, causing high ice adhesion, which will be discussed in Section 3.4.

Snapshot images of the nucleation and growth of ice on Ni/PDMS-S are shown in Fig.3. The images demonstrate that ice forms discriminately over the surface from the condensed supercooled droplets. There are several condensed supercooled droplets distributed on the surface. The initiated ice crystal would grow from the bottom right corner to the central area as indicated in Fig.3b to Fig.3e. Comparing Fig.3c and Fig.3d, the area with condensed supercooled droplets is more likely to form ice. These condensed supercooled droplets would

act as the preferential ice nucleation sites and finally lead to the full coverage of ice on the surface. It is reported that the saturated water vapour pressure around the condensed supercooled droplets would always be higher than the ice-covered area at a constant temperature. Because of this, some of these condensed supercooled droplets would evaporate and migrate into the ice crystal, which could form ice bridges toward the condensates [28]. If an ice bridge touches the nearby condensed droplets, the supercooled droplets would freeze much quickly. The phenomenon could be explained by Wegener-Bergeron-Findeisen process in meteorology: the propagation characteristic of ice crystal which comes from the saturated water vapour pressure difference between the formed ice and the supercooled droplets [29]. Due to the flattened and reduced surface cavities, the formed ice block would have much less contact area on the sample surface, which could also be favourable for reducing the ice adhesion.

With reduced environmental humidity, sublimation would occur and ice diminishment takes place. Fig.4 shows the diminishment process of ice on both Ni/PDMS-A and Ni/PDMS-S. It could be observed that the surface morphology of Ni/PDMS-A maintains intact when the ice crystal recedes during the sublimation. In Fig.4a, the ice around the sharp and deep surface pores would diminish along with the directions indicated by the red arrows. From Fig.4b to Fig.4c, the anchoring of ice into the sharp and deep surface pores is clearly observed, as shown in the red circles of the embedded anchored ice. While for Ni/PDMS-S, the ice layer becomes thinner and the edge changes from rounded to angular as indicated from Fig.4d to Fig.4e. The icing area has also moved a bit upper from Fig.4d to Fig.4e. The disappearance of the formed ice crystal is just opposite to its propagation direction. Unlike Ni/PDMS-A, there is no ice anchoring or retardation observed during the whole process, indicating good potential in de-icing.

3.4 Ice adhesion strength of the samples

Fig.5a shows the ice adhesion results of AR-Ni, Ni/PDMS-S, and Ni/PDMS-A. The results of 304 SS substrates and SS-PDMS are also given as references. The thickness of the prepared PDMS layer on SS/PDMS was around 40 μm. The columns represent the ice adhesion strengths, indicating how easy the formed ice could be removed from the studied surface. Icing is an inevitable process under the condition of sufficient supercooling [30]. The ice adhesion strength on the 304 SS substrates is 94.3±4.30 kPa, while for AR-Ni, the value is 56.9±5.22 kPa. This indicates that the ice forms on the Ni foam skeleton conforming to the Cassie-Baxter state. The trapped air pockets at the Cassie-Baxter interface could act as the stress concentrators. And it could further help to generate cracks and cause a reduction in the ice adhesion. But the Ni foam skeleton might not reduce the ice adhesion strength effectively because the initial Cassie-Baxter state could be damaged under supercooled airflow condition, which produces a strong action of mechanical interlock between ice and solid surface [31]. Ice adhesion strength is largely related to hydrogen bonding, van der Waals forces, and electrostatic interaction. Among them, the electrostatic interaction could be the dominant factor [32]. Icephobic coating with high surface energy would increase the electrostatic interaction between ice and the coating surface. The ice adhesion value of SS-PDMS is only 5.62±1.55 kPa, indicating good de-icing performance, which is contributed by the low elastic modulus and low surface free energy of PDMS. For Ni/PDMS-A, the ice adhesion strength increases to 19.6±2.90 kPa. The reason may come from that ice accretion could occur inside the sharp and deep surface pores and introduce mechanical interlocks. Then the ice adhesion strength of Ni/PDMS-S is also very low, only 5.85±1.51 kPa. The smooth and shallow surface cavities help to reduce the volume of mechanical interlock ice. The low ice adhesion strength could be explained by the microscopic crack initiation mechanism derived from the small surface cavities and the difference in elastic modulus between Ni foam skeleton and PDMS filling during the ice

detachment, as indicated by the schematic diagram in Fig.5b. The randomly distributed triangles refer to the cross-sectional structures of Ni foam skeleton, as observed in Fig.1b, while the other areas are occupied by PDMS filling. The difference in stress concentration and elastic modulus would result in different micro-distortions. This would prompt the generation of microscopic cracks along with the ice-layer interface. These initiated cracks would promote the ice fracture at the ice/solid interface thus lower the ice adhesion. The incompatibility of interface deformation and the stiffness inhomogeneity at the ice/solid interface help to induce the crack initiation mechanism [33]. The smooth and shallow surface cavities would effectively maintain the low ice adhesion on Ni/PDMS-S, which has been verified by the experimental results.

3.5 De-icing performance via electro-thermal heating test

The electro-thermal de-icing test was conducted to evaluate the overall de-icing performance of the samples. In this testing model, heat transfer is perceived as a one-dimensional flux from the heating side to the ice/sample interface. The energy used to melt the interface ice is directly linked to ice adhesion strength and thermal conduction efficiency [23]. The total thermal resistances consist of a sum of reciprocal conductivities and could be determined by considering each layer in series. The total effective thermal conductivity k_{eff} could be calculated using equation (3) [34]:

$$k_{eff} = \frac{\sum b}{\sum_{n=1}^{\infty} \frac{b_n}{k}} \tag{3}$$

Where $\sum b$ is the overall thickness of the multi-lamina panels, and $\sum b/k_{eff}$ refers to the overall heat transfer resistance per unit area. The temperatures at different layers can be calculated using a simple form of Fourier Law:

$$q = \frac{\Delta T}{R_{th}} \tag{4}$$

$$R_{th} = \frac{L}{A \cdot k} \tag{5}$$

Where q is the heat flux, ΔT is the temperature difference between two layers, R_{th} is the thermal resistance, L is the layer thickness, A is the conduction area, and k is the thermal conductivity of the material. If one layer possesses poor thermal conductivity, it contributes more to the total heat resistance and further affects the heat conduction of the whole system.

In the experiment, the only variant is the surface layer of the samples, and all of the other elements are kept the same. The temperature changing curves during the tests are shown in Fig.6, corresponding to AR-Ni, Ni/PDMS-A and Ni/PDMS-S, respectively. There are two key experimental outputs: the melting duration for ice detachment and the detected temperature versus heating time. The temperatures at the end of the curves indicate the differences in thermal conduction on samples during the electro-thermal heating [23]. The three curves show similar changing trends. The slope of the curves at certain points could reflect the heat conduction efficiency of the surface layers or coatings. Samples with higher thermal conductivity possess higher heat flow per unit time. They all have reached flat trends at the end of the curves, meaning that a balance between the decalescence from ice melting and heat flow was established before the detachment of the ice cube. The attached ice would keep melting during the test. When the ice adhesion at the interface is no longer strong enough to against the gravity of the ice cube, the ice cube would then detach. The overall energy input could be calculated.

The real-time temperature of AR-Ni is the highest in the same duration among the three samples, and its final detachment temperature is also the highest, 6.69±0.22 °C. The time used for ice detachment is also the longest, 1416±14 s, as seen in Tab.2. The reason for the long detachment duration could be ascribed to the serious mechanical interlock caused by the porous

surface structure, and the low thermal conductivity of the Ni foam which has around 90% porosity filled by air (the thermal conductivity of air is only 0.024 W·m/K at 0 ℃). For Ni/PDMS-A, the temperature curve sits in the middle, with the final detachment at 6.23±0.07 ℃ and the detachment duration reduces to 1037±10 s. Because of the introduction of PDMS layer, some of the surface porosity has been covered, significantly reducing the mechanical interlock effect on the surface. Also, the PDMS filling which replaces some air helps to reduce the overall thermal resistance of the samples (the thermal conductivity of pure PDMS is 0.15 W·m/K). So the ice detachment duration is shortened and the final detachment temperature is also lowered compared to those of AR-Ni. Ni/PDMS-S has the quickest ice detachment of 788±6 s and the lowest detachment temperature 5.29±0.18 ℃. The thermal energy required to melt the interface ice mainly depends on the extent of mechanical interlock and the surface ice adhesion. Due to the flattened and shallow surface cavities, the mechanical interlock would be much reduced on the surface of Ni/PDMS-S, which is also evidenced by the low ice adhesion. With much lower surface porosities, the overall thermal resistance of Ni/PDMS-S would also be significantly reduced. By considering the two factors, the total thermal energy efficiency is increased. For the design of icephobic coatings, low thermal resistance is an essential requirement for hybrid ice protection involving heating, when the target is to minimise energy consumption [23]. Ni/PDMS-S has demonstrated much-improved performance to satisfy such requirements.

3.6 Evaluation of durability

An important consideration for practical applications of icephobic materials is the stability against mechanical and environmental impacts [35]. Therefore, the durability performance of the icephobic materials needs to be evaluated.

The 3D topography images and SEM images of the three samples before and after water-sand impinging tests are shown in Fig.S4 and Fig.S5 (Supplementary Material). For SS-PDMS, it is clearly observed that some cracks form on the surface, as indicated in Fig.S5b (Supplementary Material). During the impinging, the water/sand abrasives continuously attack the coating surface, causing the formation of cracks and surface roughening. Rough hump structures could be found on the 3D topography images in Fig.S4b (Supplementary Material). Due to the "scratch effect" of the sands on the soft PDMS surface during the erosion, the impinging water-sand suspension could create some surface damage. The roughness value Ra also increases from 0.4±0.01 μm to 0.9±0.04 μm. For Ni/PDMS-S and Ni/PDMS-A, only a very little surface change could be observed, as shown in Fig.S4 and Fig.S5 (Supplementary Material). Such change on the surface is mainly attributed to the scratch effect from the erosion of the sand particles. The surface of Ni/PDMS-S nearly remains unchanged after erosion, and no crack and hump structure appear, showing good erosion resistance. It is found that the water-sand suspension impinging only causes some tiny craters on the sample surface after the erosion.

Fig.7 shows the ice adhesion strength of different samples before and after water-sand impinging tests. The value of AR-Ni 56.9±5.22 kPa is listed as a reference. The ice adhesion strength of as-prepared SS-PDMS layer sample has a sharp increase from 5.62±1.55 kPa to over 32.3±2.74 kPa after the water-sand impinging test. This is mainly ascribed to the mechanical interlock derived from the formed cracks and roughened surface structure, as shown in Fig.S5a and Fig.S5b (Supplementary Material). For Ni/PDMS-A, the value increases from 19.6±2.90 kPa to 34.2±2.61 kPa. The Ni foam skeleton protects the surface from the water/sand erosion, as no cracks is formed according to the surface observation, such increase is mainly attributed to the surface roughening effects from the sand scratch during the erosion. For Ni/PDMS-S, the ice adhesion strength slightly increases from 5.85±1.55 kPa to 7.05±0.93

kPa after the water-sand impinging test, demonstrating great improvement on druability. Compared to Ni/PDMS-A, Ni/PDMS-S could avoid the mechanical interlock of ice due to the flattening surface feature, maintaining the low ice adhesion after the erosion. Moreover, the micro-crack initiation mechanism initiated by the small surface cavities would effectively prompt the ice removal with low external load.

Fig.8a shows the schematic analysis of shock wave propagation process on Ni/PDMS-S during the water-sand impinging test. With the water-sand impacts on the layer surface, the impinging water droplet shows a compressed shape while the sand particle remains its original geometry. The impact abrasion and direct shear abrasion brought by the impinging sand particles during the impingement would be reduced by the Ni foam/PDMS structure effectively. The synergy impact of the water-sand mixture onto a solid surface is quite complex, and the interaction of the waves generated during the impingement will depend upon the impact conditions and material properties [36]. The compressional waves in the longitudinal direction would be initiated and propagate to the whole layer (showing as the orange hemisphere), and then the transverse shear waves would form and spread along with the skeleton inside the layer (showing as the smaller red hemisphere). The pressure generated during the impingement refers to the water-hammer pressure and the magnitude varies depending on the acoustic properties of the target material and the liquid [37]. During the impingement, the maximum pressure would have some delay after the initial shockwave generated by the impact reaches the contact circle edge [38]. Maximum shear stresses are normally observed on these radial locations. With the continuous consecutive water-sand mixture impact, the reflected waves occur and could produce tensile stress (showing as the bottom green planar). Combined with the deformation of the impinging water droplet, the impact from the impingement results in the formation of the third wave, Rayleigh wave, which is confined to the layer surface and shows in an elliptical motion. Under normal circumstances, the erosion failure of the surface layer could be initiated

by a local imbalance of tensile and shear stresses in regions of direct impact area [39]. But in the Ni foam/PDMS layer structure, the stress could be reduced when transmitted inside the Ni/PDMS layer due to the relative acoustic impedance effect [40]. The propagation of the post-impact shock wave could also be limited by the elastic and viscoelastic responses of the Ni/PDMS layer [39]. The Ni skeleton would help to reduce the local damage and transfer and limit the different wave propagations, build a balance between the tensile and shear stresses, increasing the erosion resistance and avoiding the erosion failure.

Fig.8b shows the impact shock from water-sand suspension impingement on the Ni foam/PDMS structure. It indicates that the impact abrasion could be significantly restrained and the impact energy could be transferred to a much larger area through the Ni skeleton. And the PDMS filling, which is a highly-damped, visco-elastic polymer, also helps such transfer and absorb most of the energy. Therefore, the Ni foam/PDMS structure could be well maintained under the severe impact abrasion and direct shear abrasion, leading to the remarkable increase in the erosion resistance. The Ni foam skeleton would also act as the armours for the filled PDMS, against possible mechanical scratch and removal from the high-velocity water droplets and sharp SiC particles. Compared with other recently reported icephobic coatings, the mechanical durability of Ni foam/PDMS layer is quite impressive. The details of the comparison are provided in Tab. S1 (Supplementary Material). In comparison, the ice adhesion strength of Ni/PDMS two-phase layer remains at a very low level after the water-sand impinging test, indicating good durability on the erosion resistance.

4. Conclusions

In summary, this work developed a new type of highly durable icephobic layer structure based on a concept of combining robust porous metallic skeleton and icephobic filling. With

the help of icephobic PDMS layer and micro-crack initiation mechanism, the two-phase Ni foam/PDMS layer structures with fine surface cavities demonstrated very low ice adhesion strength of only 7.05 kPa after erosion impact, which shows promising prospects in de-icing aspects. The layer structure could further satisfy the requirement of passive ice removal on airplane wings or power lines ($<$ 20 kPa) [5]. The micro-crack initiation along with the ice/structure interface mainly came from the fine surface cavities and the difference in elastic modulus between the ice and the PDMS filling. Ice growth and diminishment on the Ni foam/PDMS layer was studied using ESEM, confirming good icephobicity of the two-phase structures. Furthermore, a comparison table of durability assessment between the Ni/PDMS layer and other recently reported studies has been summarised in Tab.S1 (Supplementary Material) [41-43]. Although there is still a lack of universal standards for the durability evaluation [44], useful comparisons could be made based on the presented data. The Ni foam/PDMS layer remained stable under severe water-sand impinging erosion and demonstrated competitive mechanical durability as compared with existing works [45-47]. The usage of Ni foam skeleton could offer better erosion protection and act as armours for the implementation of elastomers (filled PDMS). With the stable layer construction, the micro-crack initiation mechanism could ensure continuity of effectiveness in ice removal. The energy efficiency of the Ni foam/PDMS layer in the electro-thermal de-icing test has also been improved, indicating that the new two-phase structural design could be a promising approach for hybrid ice protection with low energy consumption.

By combining the advantages of mechanical durability of Ni foam skeleton and icephobic performance of PDMS layer, the newly developed two-phase layer construction offers excellent icephobicity with significant improvement in mechanical durability. For example, icephobic gummed tape may be developed based on the two-phase layer and a gummed tape, which can be directly attached to component surfaces such as aeroplane wings

or wind turbines for ice protection purposes. It has the good potential to satisfy the ice protection requirement of flexibility, lightweight, scalable, and long icing delay time with good anti-icing and de-icing performances [48, 49]. The use of the fabricated Ni foam/PDMS layer would provide an innovative solution for ice protection and other areas related to surface hydrophobicity. The design concept of combining robust substrate skeleton and icephobic filling could provide new insight into the design principles of icephobic surfaces.

Acknowledgments: The work is supported by a joint Ph.D. studentship between China Scholarship Council (CSC) and The University of Nottingham. The authors acknowledge the use of facilities at Nanoscale and Microscale Research Centre of the University of Nottingham, this research was supported in part by the Engineering and Physical Sciences Research Council [grant number EP/L022494/1], as well as University of Nottingham Propulsion Futures Beacon for funding under Grant PF020. The authors thank Dr. Barbara Turnbull at University of Nottingham for assistance with ice adhesion strength test.

Author Contributions

J.W. prepared the samples and conducted the experiments. M.J.W. and J.P.L. helped with the icephobicity tests. F.X., T.H. and C.S. contributed to the experiment design and the manuscript writing. X.H.H. initiated this work. J.W. and X.H.H. co-wrote the manuscript. All authors contributed to the discussion and reviewed the manuscript.

Declaration of Competing Interest

The authors declare no competing financial interest.

References:

[1] Kreder MJ, Alvarenga J, Kim P, Aizenberg J. Design of anti-icing surfaces: smooth, textured or slippery? Nature Reviews Materials. 2016;1:15003.
[2] Golovin K, Dhyani A, Thouless M, Tuteja A. Low-interfacial toughness materials for effective large-scale deicing. Science. 2019;364:371-5.
[3] Qing Y, Long C, An K, Hu C, Liu C. Sandpaper as template for a robust superhydrophobic surface with self-cleaning and anti-snow/icing performances. Journal of colloid and interface science. 2019;548:224-32.
[4] He Z, Zhuo Y, He J, Zhang Z. Design and preparation of sandwich-like polydimethylsiloxane (PDMS) sponges with super-low ice adhesion. Soft Matter. 2018;14:4846-51.
[5] Golovin K, Kobaku SP, Lee DH, DiLoreto ET, Mabry JM, Tuteja A. Designing durable icephobic surfaces. Science advances. 2016;2:e1501496.
[6] Cui W, Pakkanen TA. Icephobic performance of one-step silicone-oil-infused slippery coatings: Effects of surface energy, oil and nanoparticle contents. Journal of colloid and interface science. 2020;558:251-8.
[7] Wen M, Wang L, Zhang M, Jiang L, Zheng Y. Antifogging and icing-delay properties of composite micro-and nanostructured surfaces. ACS applied materials & interfaces. 2014;6:3963-8.
[8] Guo P, Zheng Y, Wen M, Song C, Lin Y, Jiang L. Icephobic/anti-icing properties of micro/nanostructured surfaces. Advanced Materials. 2012;24:2642-8.
[9] Xu Y, Zhang G, Li L, Xu C, Lv X, Zhang H, et al. Icephobic behaviors of superhydrophobic amorphous carbon nano-films synthesized from a flame process. Journal of colloid and interface science. 2019;552:613-21.
[10] Meuler AJ, McKinley GH, Cohen RE. Exploiting topographical texture to impart icephobicity. ACS nano. 2010;4:7048-52.
[11] Zhuo Y, Wang F, Xiao S, He J, Zhang Z. One-step fabrication of bioinspired lubricant-regenerable icephobic slippery liquid-infused porous surfaces. ACS omega. 2018;3:10139-44.
[12] Wong T-S, Kang SH, Tang SK, Smythe EJ, Hatton BD, Grinthal A, et al. Bioinspired self-repairing slippery surfaces with pressure-stable omniphobicity. Nature. 2011;477:443-7.
[13] Xiao L, Li J, Mieszkin S, Di Fino A, Clare AS, Callow ME, et al. Slippery liquid-infused porous surfaces showing marine antibiofouling properties. ACS applied materials & interfaces. 2013;5:10074-80.
[14] Mahmut T, Memon H, Xu F, Ahmed I, Hou X. Electrospun nanofibre membrane based transparent slippery liquid-infused porous surfaces with icephobic properties. Colloids and Surfaces A: Physicochemical and Engineering Aspects. 2020;585:124177.
[15] Kim P, Wong T-S, Alvarenga J, Kreder MJ, Adorno-Martinez WE, Aizenberg J. Liquid-infused nanostructured surfaces with extreme anti-ice and anti-frost performance. ACS nano. 2012;6:6569-77.
[16] Irajizad P, Hasnain M, Farokhnia N, Sajadi SM, Ghasemi H. Magnetic slippery extreme icephobic surfaces. Nature communications. 2016;7:1-7.
[17] Wexler JS, Jacobi I, Stone HA. Shear-driven failure of liquid-infused surfaces. Physical review letters. 2015;114:168301.
[18] Rykaczewski K, Anand S, Subramanyam SB, Varanasi KK. Mechanism of frost formation on lubricant-impregnated surfaces. Langmuir. 2013;29:5230-8.
[19] Zhuo Y, Håkonsen V, He Z, Xiao S, He J, Zhang Z. Enhancing the mechanical durability of icephobic surfaces by introducing autonomous self-healing function. ACS applied materials & interfaces. 2018;10:11972-8.
[20] Wang D, Sun Q, Hokkanen MJ, Zhang C, Lin F-Y, Liu Q, et al. Design of robust superhydrophobic surfaces. Nature. 2020;582:55-9.
[21] Irajizad P, Al-Bayati A, Eslami B, Shafquat T, Nazari M, Jafari P, et al. Stress-localized durable icephobic surfaces. Materials Horizons. 2019;6:758-66.
[22] Esmaeili AR, Mir N, Mohammadi R. A facile, fast, and low-cost method for fabrication of micro/nano-textured superhydrophobic surfaces. Journal of Colloid and Interface Science. 2020;573:317-27.

[23] Zheng Y, Wang J, Liu J, Choi K-S, Hou X. Energy saving strategy for the development of icephobic coatings and surfaces. Thin Solid Films. 2019;687:137458.
[24] Janjua ZA. The influence of freezing and ambient temperature on the adhesion strength of ice. Cold Regions Science and Technology. 2017;140:14-9.
[25] Liu J, Wang J, Mazzola L, Memon H, Barman T, Turnbull B, et al. Development and evaluation of poly (dimethylsiloxane) based composite coatings for icephobic applications. Surface and Coatings Technology. 2018;349:980-5.
[26] Wang J, Memon H, Liu J, Yang G, Xu F, Hussain T, et al. Effect of surface adsorption on icing behaviour of metallic coating. Surface and Coatings Technology. 2019;380:125068.
[27] Wang J, Liu J, Neate N, Bai M, Xu F, Hussain T, et al. Investigation on time-dependent wetting behavior of Ni-Cu-P ternary coating. Journal of Alloys and Compounds. 2018;765:221-8.
[28] Boreyko JB, Collier CP. Delayed frost growth on jumping-drop superhydrophobic surfaces. ACS nano. 2013;7:1618-27.
[29] Kim M-H, Kim H, Lee K-S, Kim DR. Frosting characteristics on hydrophobic and superhydrophobic surfaces: A review. Energy Conversion and Management. 2017;138:1-11.
[30] Zou M, Beckford S, Wei R, Ellis C, Hatton G, Miller M. Effects of surface roughness and energy on ice adhesion strength. Applied Surface Science. 2011;257:3786-92.
[31] Nosonovsky M, Hejazi V. Why superhydrophobic surfaces are not always icephobic. ACS nano. 2012;6:8488-91.
[32] Jung S, Tiwari MK, Doan NV, Poulikakos D. Mechanism of supercooled droplet freezing on surfaces. Nature communications. 2012;3:615.
[33] He Z, Xiao S, Gao H, He J, Zhang Z. Multiscale crack initiator promoted super-low ice adhesion surfaces. Soft matter. 2017;13:6562-8.
[34] Holman JP. Heat transfer: McGraw-hill Higher Education; 2010.
[35] Liu F, Pan Q. Facile fabrication of robust ice-phobic polyurethane sponges. Advanced Materials Interfaces. 2015;2:1500219.
[36] Keegan MH, Nash D, Stack M. On erosion issues associated with the leading edge of wind turbine blades. Journal of Physics D: Applied Physics. 2013;46:383001.
[37] Cook SS. Erosion by water-hammer. Proceedings of the Royal Society of London Series A, Containing Papers of a Mathematical and Physical Character. 1928;119:481-8.
[38] Zahavi J, Nadiv S, Schmitt Jr G. Indirect damage in composite materials due to raindrop impact. Wear. 1981;72:305-13.
[39] Cortés E, Sánchez F, O'Carroll A, Madramany B, Hardiman M, Young TM. On the material characterisation of wind turbine blade coatings: the effect of interphase coating-laminate adhesion on rain erosion performance. Materials. 2017;10:1146.
[40] Springer GS, Yang C-I, Larsen PS. Analysis of rain erosion of coated materials. Journal of Composite Materials. 1974;8:229-52.
[41] Zhang Y, Ge D, Yang S. Spray-coating of superhydrophobic aluminum alloys with enhanced mechanical robustness. Journal of colloid and interface science. 2014;423:101-7.
[42] Wang N, Xiong D, Pan S, Wang K, Shi Y, Deng Y. Robust superhydrophobic coating and the anti-icing properties of its lubricants-infused-composite surface under condensing condition. New Journal of Chemistry. 2017;41:1846-53.
[43] Mobarakeh LF, Jafari R, Farzaneh M. Robust icephobic, and anticorrosive plasma polymer coating. Cold Regions Science and Technology. 2018;151:89-93.
[44] Shen Y, Wu X, Tao J, Zhu C, Lai Y, Chen Z. Icephobic materials: Fundamentals, performance evaluation, and applications. Progress in Materials Science. 2019;103:509-557.
[45] Nanda D, Varshney P, Satapathy M, Mohapatra SS, Bhushan B, Kumar A. Single step method to fabricate durable superliquiphobic coating on aluminum surface with self-cleaning and anti-fogging properties. Journal of colloid and interface science. 2017;507:397-409.
[46] Chen J, Dou R, Cui D, Zhang Q, Zhang Y, Xu F, et al. Robust prototypical anti-icing coatings with a self-lubricating liquid water layer between ice and substrate. ACS applied materials & interfaces. 2013;5:4026-30.
[47] Wu X, Zhao X, Ho JWC, Chen Z. Design and durability study of environmental-friendly room-temperature processable icephobic coatings. Chemical Engineering Journal. 2019;355:901-9.

[48] Wang L, Wen M, Zhang M, Jiang L, Zheng Y. Ice-phobic gummed tape with nano-cones on microspheres. Journal of Materials Chemistry A. 2014;2:3312-6.
[49] Niemelä-Anttonen H, Kiilakoski J, Vuoristo P, Koivuluoto H. Icephobic Performance of Different Surface Designs and Materials. Proceedings of the International Workshop on Atmospheric Icing of Structures, IWAIS2019.

List of Figure Captions

Fig. 1. SEM images of (a) surface morphology and (b) cross-sectional images of AR-Ni; (c) surface morphology of Ni/PDMS-A; (d) surface morphology of Ni/PDMS-S

Fig. 2. Water condensation and ice formation process on Ni/PDMS-A (Pressure: 2.38-2.62 torrs; Temp: -7.1 to -5.1 °C; Humidity: 83.9 - 90.5%)

Fig. 3. Ice formation process on Ni/PDMS-S (Pressure: 2.93 torrs; Temp: -5.3 °C; Humidity: 94.7%)

Fig. 4. (a-c) Anchoring of interlocked ice on Ni/PDMS-A when ice sublimates (Pressure: 1.89 torrs; Temp: -4.0 °C; Humidity: 56.3%); (d-f) Ice diminishing process on Ni/PDMS-S (Pressure: 2.07-2.36 torrs; Temp: -6.0 to -6.3 °C; Humidity: 70.4 % - 82.6 %)

Fig. 5. (a) Ice adhesion results of 304 SS, AR-Ni, SS-PDMS, Ni/PDMS-A and Ni/PDMS-S; (b) Schematic view of micro-crack initiation mechanism at the surface cavities between the ice-layer interfaces

Fig. 6. Temperature changing curves during electro-thermal tests for different samples

Fig. 7. Ice adhesion strengths of different samples versus water-sand impinging tests

Fig. 8. Schematic views of (a) shock wave propagation occurring upon impact of water-sand impingement on Ni/PDMS-S (b) re-distribution of impact energy of water-sand impingement on Ni foam/PDMS layer

Graphical Abstract

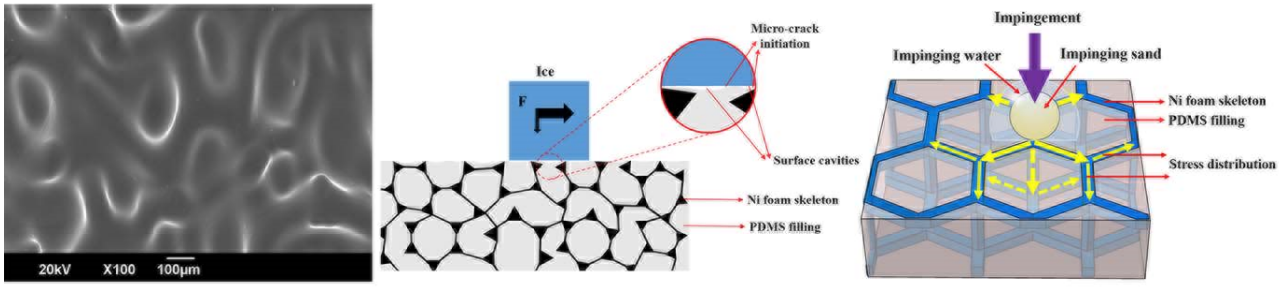

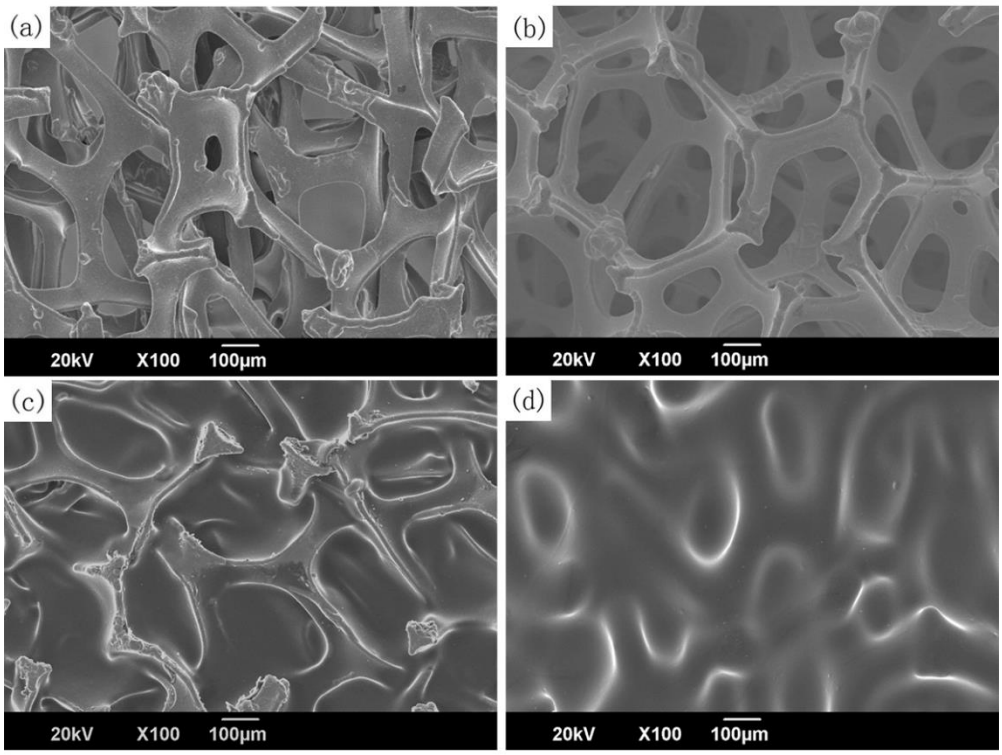

Fig. 1. SEM images of (a) surface morphology and (b) cross-sectional images of AR-Ni; (c) surface morphology of Ni/PDMS-A; (d) surface morphology of Ni/PDMS-S

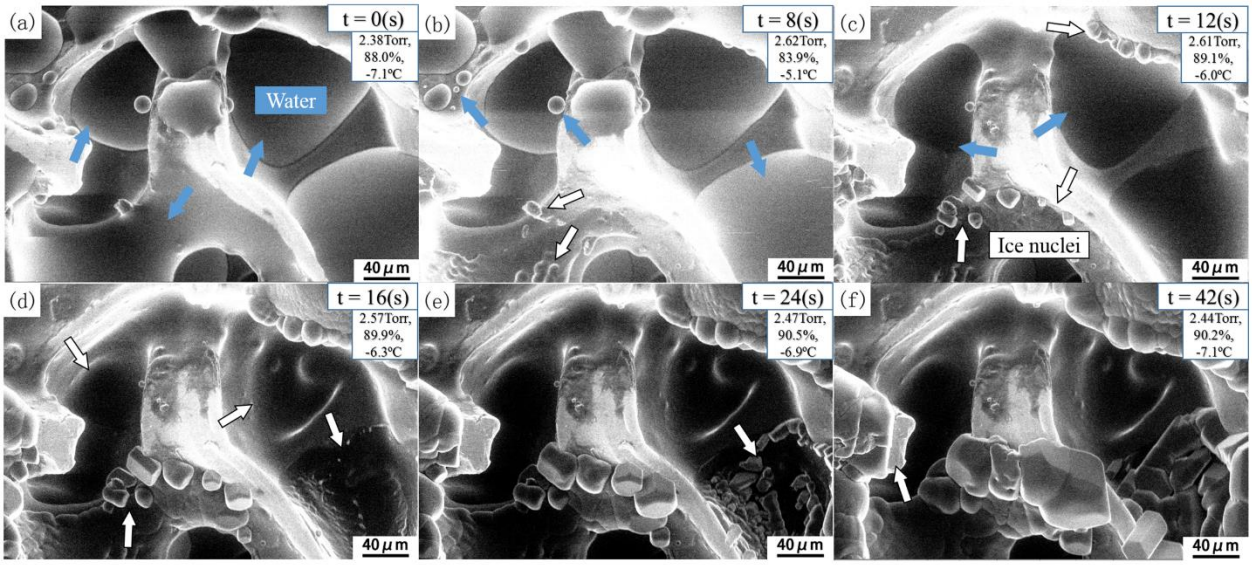

Fig. 2. Water condensation and ice formation process on Ni/PDMS-A (Pressure: 2.38-2.62 torrs; Temp: -7.1 to -5.1 °C; Humidity: 83.9 - 90.5%)

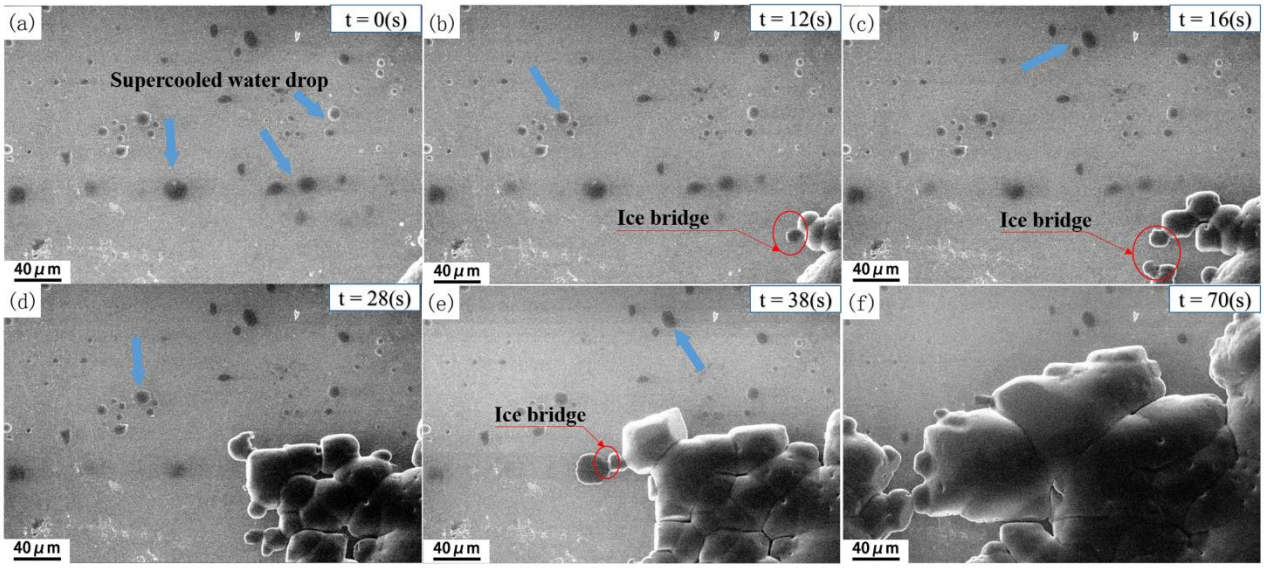

Fig. 3. Ice formation process on Ni/PDMS-S (Pressure: 2.93 torrs; Temp: -5.3 °C; Humidity: 94.7%)

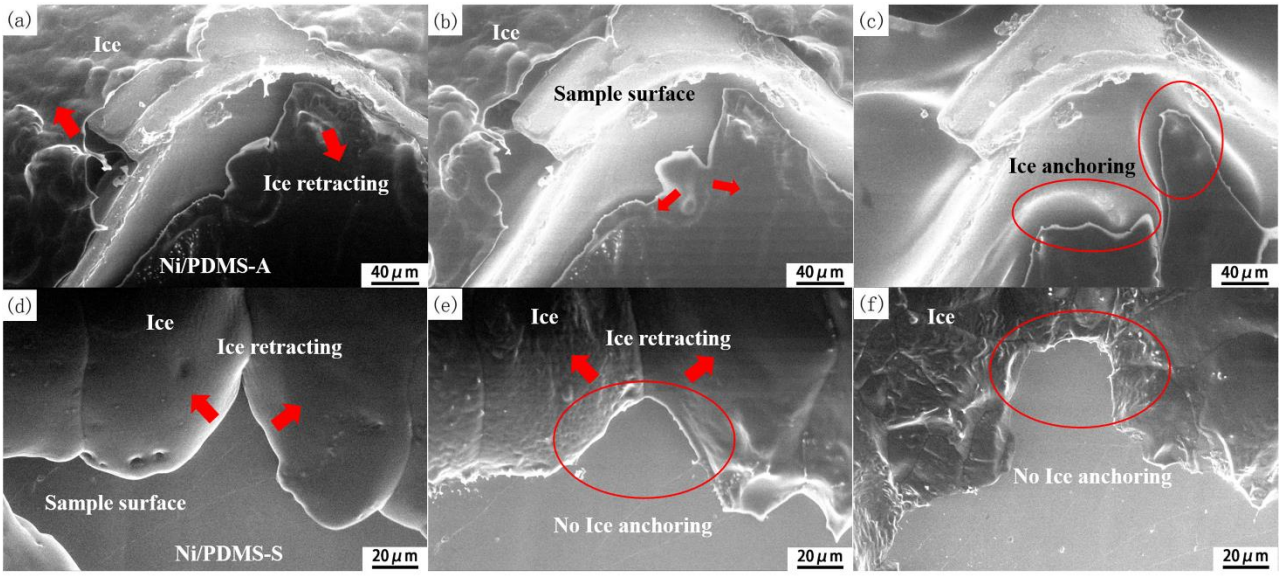

Fig. 4. (a-c) Anchoring of interlocked ice on Ni/PDMS-A when ice sublimates (Pressure: 1.89 torrs; Temp: -4.0 °C; Humidity: 56.3%); (d-f) Ice diminishing process on Ni/PDMS-S (Pressure: 2.07-2.36 torrs; Temp: -6.0 to -6.3 °C; Humidity: 70.4 % - 82.6 %)

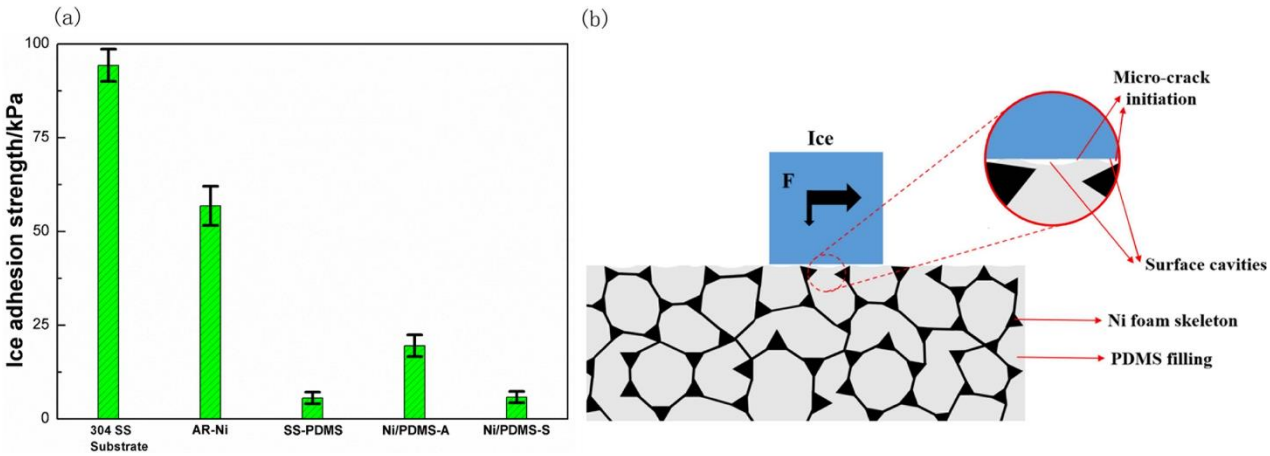

Fig. 5. (a) Ice adhesion results of 304 SS, AR-Ni, SS-PDMS, Ni/PDMS-A and Ni/PDMS-S; (b) Schematic view of micro-crack initiation mechanism at the surface cavities between the ice-layer interfaces

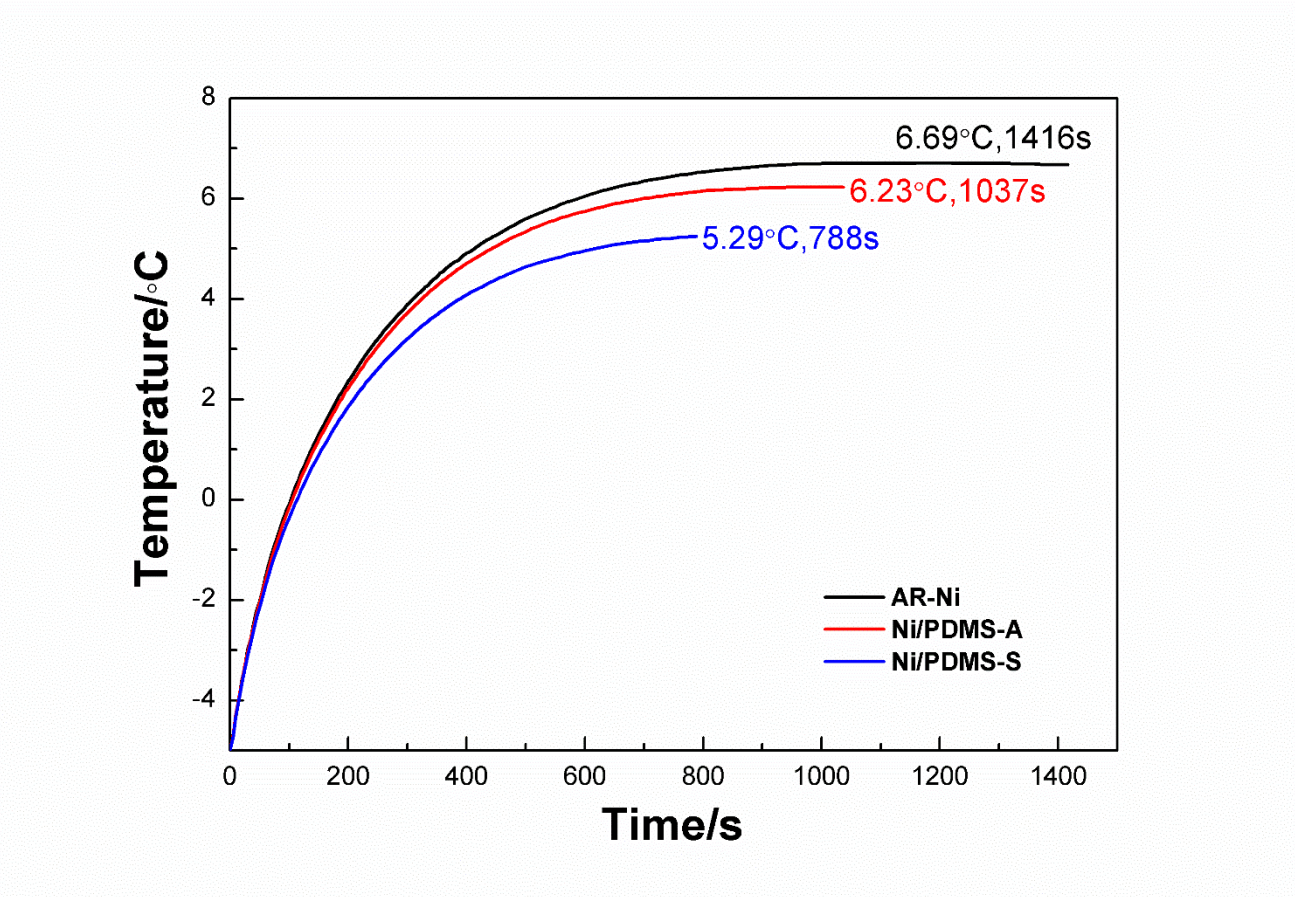

Fig. 6. Temperature changing curves during electro-thermal tests for different samples

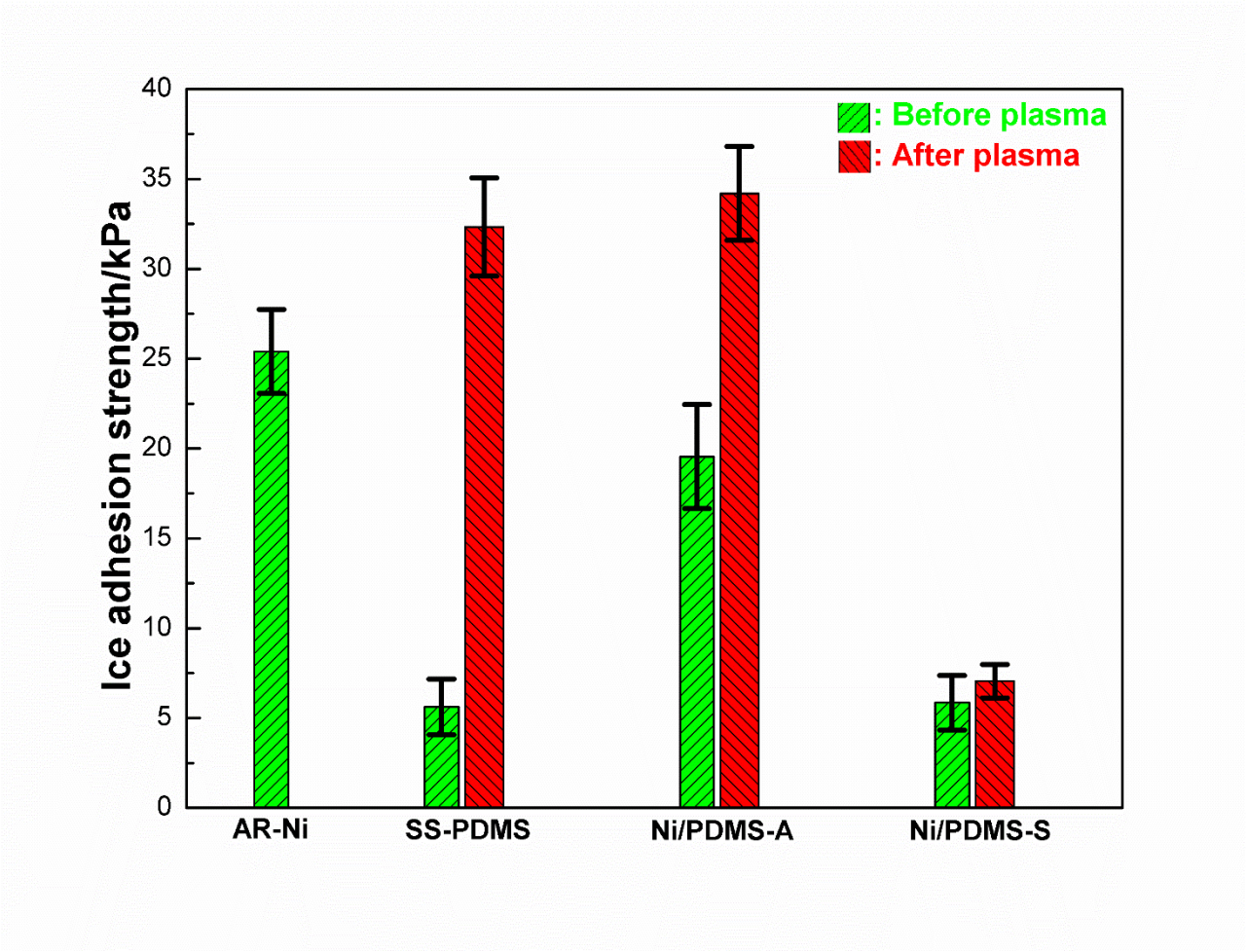

Fig. 6. Temperature changing curves during electro-thermal tests for different samples

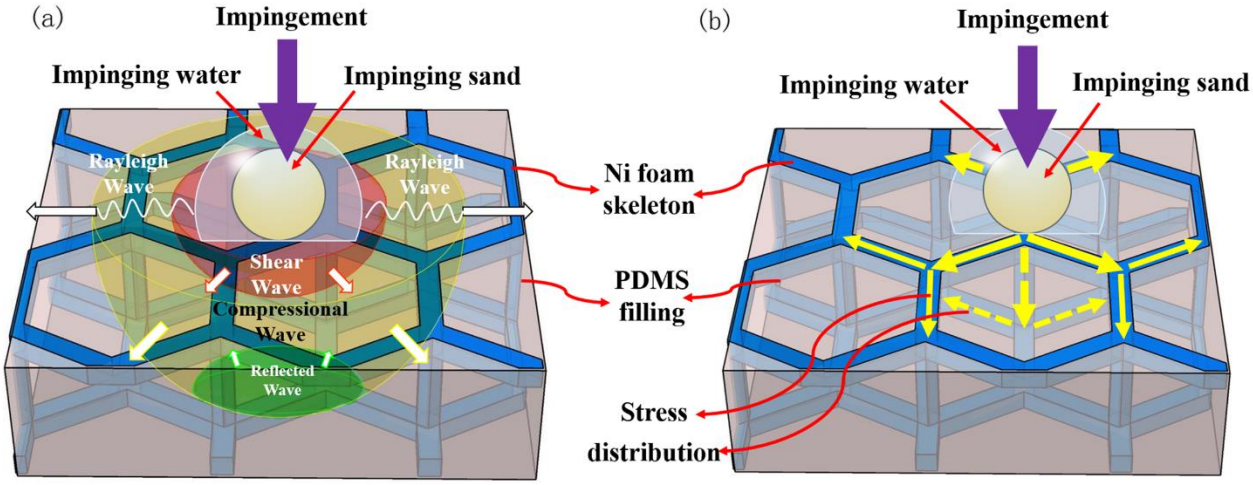

Fig. 8. Schematic views of (a) shock wave propagation occurring upon impact of water-sand impingement on Ni/PDMS-S (b) re-distribution of impact energy of water-sand impingement on Ni foam/PDMS layer

List of Table Captions

Tab. 1.

Samples	WCA/°	Adv/°	Rec/°	CAH/°
AR-Ni	131.4±3.2	133.1±3.7	125.2±2.8	7.8±0.1
Ni/PDMS-A	121.9±2.5	123.2±2.6	114.7±2.1	8.5±0.1
Ni/PDMS-S	112.9±2.4	113.9±1.9	99.8±1.2	14.1±0.1
Flat PDMS	110.6±2.3	114.3±1.7	98.1±1.6	16.2±0.3

Tab. 2.

Samples	Detachment temperature (°C)	Detachment time (s)	Energy consumption (J)
AR-Ni	6.69±0.22	1416±14	4050±40
Ni/PDMS-A	6.23±0.07	1037±10	2966±29
Ni/PDMS-S	5.29±0.18	788±6	2254±17